

A DLM/FD/IB Method for Simulating Cell/Cell and Cell/Particle Interaction in Microchannels**

Tsorng-Whay PAN* Lingling SHI* Roland GLOWINSKI*

(Dedicated to Professor Roger Temam on the Occasion of his 70th Birthday)

Abstract A spring model is used to simulate the skeleton structure of the red blood cell (RBC) membrane and to study the red blood cell (RBC) rheology in Poiseuille flow with an immersed boundary method. The lateral migration properties of many cells in Poiseuille flow have been investigated. The authors also combine the above methodology with a distributed Lagrange multiplier/fictitious domain method to simulate the interaction of cells and neutrally buoyant particles in a microchannel for studying the margination of particles.

Keywords Red blood cells, Elastic spring model, Margination, Fictitious domain method, Immersed boundary method, Microchannel

2000 MR Subject Classification 76Z05, 76M10

1 Introduction

The microcirculation, which is comprised of the microvessels of diameter smaller than 100 μm , is essential to the human body, since it is the location where exchange of mass and energy takes place. At the microcirculatory level, the particulate nature of the blood becomes significant. The rheological property of the red blood cells (RBCs) is a key factor of the blood flow characteristics in microvessels due to their large volume fraction (40-45%), so called hematocrit (Hct), in the whole blood. In a microvessel, RBCs tend to move to the center of the vessel so that there is a cell-free layer near the vessel wall. The non-uniform distribution of hematocrit within the cross-section of the vessel is the physical reason of Fahraeus-Lindqvist effect (see [16]) which is characterized by a decrease in the apparent blood viscosity in such microvessels.

Nowadays, *in silico* mathematical modeling and numerical study of RBC rheology have attracted growing interest (see, e.g., [8, 34]), since it is difficult to deal with *in vivo* and *in vitro* experiments on studying microcirculation and RBC rheology due to the size limitation. For example, in [15], an immersed boundary method was used to simulate 3D capsule and RBCs in shear flow with both neo-Hookean and Skalak models for membrane deformation. It was found that the bending resistance must be included in order to simulate complex shape

Manuscript received May 31, 2010. Published online October 22, 2010.

*Department of Mathematics, University of Houston, Houston, TX 77204, USA.

E-mail: pan@math.uh.edu lingling@math.uh.edu roland@math.uh.edu

**Project supported by the National Science Foundation of the United States (Nos. ECS-9527123, CTS-9873236, DMS-9973318, CCR-9902035, DMS-0209066, DMS-0443826, DMS-0914788).

of RBCs when they deform in shear flow. In [4], an immersed boundary method and a neo-Hookean model with and without bending resistance were used to simulate the interaction of two deformable cells in a shear flow in two dimensions. It was found that aggregates made of deformable cells are easily breakable by a shear flow, while those made of less deformable cells are not. In [27, 28], an immersed finite element method was presented for the simulation of RBCs in three dimensions while the RBC membrane employing a Mooney-Rivlin model. The microscopic mechanism of RBC aggregation has been linked to the macroscopic blood viscosity via direct numerical simulation and the relation between the effective viscosity of blood flow and the diameters of capillaries has been obtained. In [36], a semi-implicit particle method combined with a spring model was used to simulate a single file of RBCs between two parallel plates for various Hct in two dimensions. The parachute shape of RBCs in capillaries and flow resistance were investigated with different Hct. In [9], an immersed boundary method based on the lattice-Boltzmann method has been developed with Skalak model for the RBC membrane. Their simulations capture RBC induced lateral platelet motion and the consequent development of a platelet concentration profile that includes an enhanced concentration within a few microns of the channel walls. In [13], a discrete model for the RBC membrane has been constructed by taking into account of the volume constraint of the RBC, the local area constraint on each triangle element from the mesh for the RBC membrane, the total area constraint of the RBC surface, the stretching force between nodes on each edge of the surface triangle element, and the preferred angle between triangle elements shared a common edge (the bending resistance). These constraints give different forces acting on the nodes on the RBC surface. A lattice-Boltzmann method was combined with this discrete model to simulate 200 densely packed RBCs in three dimensional flow.

Among the methodologies and models for simulating the motion of the RBCs in flows, we want to combine the immersed boundary method with spring models since one of our main goals is to simulate the mixture of deformable and rigid particles in microvessels. For simulating rigid particles freely moving in Newtonian fluid in three dimensions, we developed very efficient methodologies, called distributed Lagrange multiplier/fictitious domain (DLM/FD) methods (see, e.g., [20, 21, 29, 30]). The DLM/FD methods are closely related to the immersed boundary methods, since they both use uniform grids on simple shape computational domain and the Lagrange multipliers play similar role as the force acting on the elastic membrane immersed in fluid for the immersed boundary methods. For modeling the RBC membrane, the general organization of the RBC membrane is well characterized. It is shown that the human RBC is a inflated closed membrane filled with a viscous fluid, called cytoplasm. The RBC membrane has a phospholipid bilayer with the attached glycocalyx at the plasmatic face of the bilayer and a network of spectrins, called the cytoskeleton, fastened to the bilayer at its cytoplasmic face (see [18, 22]). The cytoskeleton is an elastic network of spectrin which has triangular structure (and most of these triangles form hexagons) in the network (e.g., see [37]). This particular geometry, as well as the intrinsic elastic properties of the spectrin, allows the RBC to be highly deformable and elastic. Due to its special structure, the RBC membrane has strong resistance changes in area/volume and shear deformation (see [22]). Therefore, it is of significance to take into consideration the structure of the RBC membrane skeleton in the study of RBC rheology.

Several spring models (see [12–14, 22, 23, 35, 36]) were developed to illustrate the structure of the RBC membrane skeleton and to describe the deformability of the RBCs. In this paper, the mechanical properties of the RBC membrane is predicted by a elastic spring model recently proposed in [36]. We developed an immersed method combined with such elastic spring model in [38]. The fluid motion is computed using an operator splitting technique and finite element method with a fixed regular triangular mesh so faster solvers can be used for solving the fluid flow. In [38], the elastic spring model is validated by comparing with previous experimental data (see [19]), theoretical Keller and Skalak model (see [24]), and simulations (see [5, 26]) for the inclination angles and tank-treading frequencies of single RBC in shear flows.

In this paper, we test the capability of the immersed boundary method developed in [38] by applying it to simulate the motion of many RBCs in Poiseuille flow and validate it by comparing the size of the cell-free layer next to the walls with experimental and computational results. Then we combine the methodology with a distributed Lagrange multiplier/fictitious domain method to simulate the interaction of cells and neutrally buoyant particles in a microchannel (see, e.g., [17, 25], for cardiovascular and oncological applications). The computational results show that the neutrally buoyant disks behave similar to the almost circular cells when interacting with other cells. The structure of this paper is as follows: We discuss the elastic spring model and numerical methods in Section 2. In Section 3, we first study the lateral migration of many cells in Poiseuille flow and validate our method by comparing the size of the cell-free layer next to the walls. Then the numerical results of the interaction of cells and neutrally buoyant particles in a microchannel are shown. The conclusions are summarized in Section 4.

2 Models and Methods

2.1 Fictitious domain formulation

Let Ω be a bounded rectangular domain filled with blood plasma which is incompressible, Newtonian, and contains RBCs and neutrally buoyant particles with the viscosity of the cytoplasm same as that of the blood plasma (see Figure 1). We suppose, for simplicity, that Ω contains a moving neutrally buoyant rigid particle B centered at $\mathbf{G} = \{G_1, G_2\}^t$; the flow is modeled by the Navier-Stokes equations and the motion of the particle B is described by the Euler-Newton's equations. We define

$$W_{0,p} = \left\{ \mathbf{v} \mid \begin{array}{l} \mathbf{v} \in (H^1(\Omega))^2, \mathbf{v} = \mathbf{0} \text{ on the top and bottom of } \Omega \text{ and} \\ \mathbf{v} \text{ is periodic in the } x_1 \text{ direction} \end{array} \right\},$$

$$L_0^2 = \left\{ q \mid q \in L^2(\Omega), \int_{\Omega} q d\mathbf{x} = 0 \right\},$$

$$\Lambda_0(t) = \{ \boldsymbol{\mu} \mid \boldsymbol{\mu} \in (H^1(B(t)))^2, \langle \boldsymbol{\mu}, \mathbf{e}_i \rangle_{B(t)} = 0, i = 1, 2, \langle \boldsymbol{\mu}, \overrightarrow{Gx^\perp} \rangle_{B(t)} = 0 \}$$

with $\mathbf{e}_1 = \{1, 0\}^t$, $\mathbf{e}_2 = \{0, 1\}^t$, $\overrightarrow{Gx^\perp} = \{-(x_2 - G_2), x_1 - G_1\}^t$ and $\langle \cdot, \cdot \rangle_{B(t)}$ an inner product on $\Lambda_0(t)$ which can be the standard inner product on $(H^1(B(t)))^2$ (see, e.g., [21], for further information on the choice of $\langle \cdot, \cdot \rangle_{B(t)}$). Then as in [29], the fictitious domain formulation with distributed Lagrange multipliers for flow around a freely moving neutrally buoyant particle is

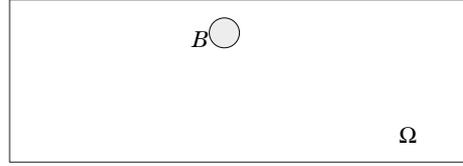


Figure 1 An example of computational domain with one rigid particle

as follows:

For a.e. $t > 0$, find $\mathbf{u}(t) \in W_{0,p}$, $p(t) \in L^2_0$, $\mathbf{V}_G(t) \in \mathbb{R}^2$, $\mathbf{G}(t) \in \mathbb{R}^2$, $\omega(t) \in \mathbb{R}$, $\boldsymbol{\lambda}(t) \in \Lambda_0(t)$ such that

$$\begin{cases} \rho \int_{\Omega} \left[\frac{\partial \mathbf{u}}{\partial t} + (\mathbf{u} \cdot \nabla) \mathbf{u} \right] \cdot \mathbf{v} \, dx + 2\mu \int_{\Omega} \mathbf{D}(\mathbf{u}) : \mathbf{D}(\mathbf{v}) \, dx - \int_{\Omega} p \nabla \cdot \mathbf{v} \, dx \\ - \langle \boldsymbol{\lambda}, \mathbf{v} \rangle_{B(t)} = \rho \int_{\Omega} \mathbf{g} \cdot \mathbf{v} \, dx + \int_{\Omega} \mathbf{f} \cdot \mathbf{v} \, dx, \quad \forall \mathbf{v} \in W_{0,p}, \end{cases} \quad (2.1)$$

$$\int_{\Omega} q \nabla \cdot \mathbf{u}(t) \, dx = 0, \quad \forall q \in L^2(\Omega), \quad (2.2)$$

$$\langle \boldsymbol{\mu}, \mathbf{u}(t) \rangle_{B(t)} = 0, \quad \forall \boldsymbol{\mu} \in \Lambda_0(t), \quad (2.3)$$

$$\frac{d\mathbf{G}}{dt} = \mathbf{V}_G, \quad (2.4)$$

$$\mathbf{V}_G(0) = \mathbf{V}_G^0, \quad \omega(0) = \omega^0, \quad \mathbf{G}(0) = \mathbf{G}^0 = \{G_1^0, G_2^0\}^t, \quad (2.5)$$

$$\mathbf{u}(\mathbf{x}, 0) = \bar{\mathbf{u}}_0(\mathbf{x}) = \begin{cases} \mathbf{u}_0(\mathbf{x}), & \forall \mathbf{x} \in \Omega \setminus \overline{B(0)}, \\ \mathbf{V}_G^0 + \omega^0 \{-(x_2 - G_2^0), x_1 - G_1^0\}^t, & \forall \mathbf{x} \in \overline{B(0)}, \end{cases} \quad (2.6)$$

where \mathbf{u} and p denote velocity and pressure, respectively, ρ is the fluid density, and μ is the fluid viscosity. We also assume that the flow is periodic in the x_1 direction with period L , L being the common length of the channel Ω . In the above (2.1)–(2.6), we have that $\mathbf{D}(\mathbf{v}) = \frac{1}{2}(\nabla \mathbf{v} + \nabla \mathbf{v}^t)$, $\boldsymbol{\lambda}$ is a Lagrange multiplier, \mathbf{g} is gravity, \mathbf{f} is a body force which is the sum of \mathbf{f}_p and \mathbf{f}_B , where \mathbf{f}_p is the pressure gradient pointing in the x_1 direction and \mathbf{f}_B accounts for the force acting on the fluid/cell interface (please see the following sections), \mathbf{V}_G is the translation velocity of the particle B , and ω is the angular velocity of the particle B . We suppose that the *no-slip* condition holds on ∂B . We also use, if necessary, the notation $\phi(t)$ for the function $\mathbf{x} \rightarrow \phi(\mathbf{x}, t)$.

Remark 2.1 In (2.3), the rigid body motion in the region occupied by the particle is enforced via Lagrange multipliers $\boldsymbol{\lambda}$. As discussed in [29], we solve the following equations to obtain the translation velocity $\mathbf{V}_G(t)$ and the angular velocity $\omega(t)$

$$\begin{cases} \langle \mathbf{e}_i, \mathbf{u}(t) - \mathbf{V}_G(t) - \omega(t) \overrightarrow{Gx^\perp} \rangle_{B(t)} = 0 \quad \text{for } i = 1, 2, \\ \langle \overrightarrow{Gx^\perp}, \mathbf{u}(t) - \mathbf{V}_G(t) - \omega(t) \overrightarrow{Gx^\perp} \rangle_{B(t)} = 0. \end{cases} \quad (2.7)$$

Remark 2.2 In (2.1), $2 \int_{\Omega} \mathbf{D}(\mathbf{u}) : \mathbf{D}(\mathbf{v}) \, dx$ can be replaced by $\int_{\Omega} \nabla \mathbf{u} : \nabla \mathbf{v} \, dx$, since \mathbf{u} is divergence free and in $W_{0,p}$. Also the gravity \mathbf{g} in (2.1) can be absorbed into the pressure term.

2.2 Elastic spring model for the RBC membrane

A two-dimensional elastic spring model used in [36] is considered in this paper to describe the deformable behavior of the RBCs. Based on this model, the RBC membrane can be viewed as

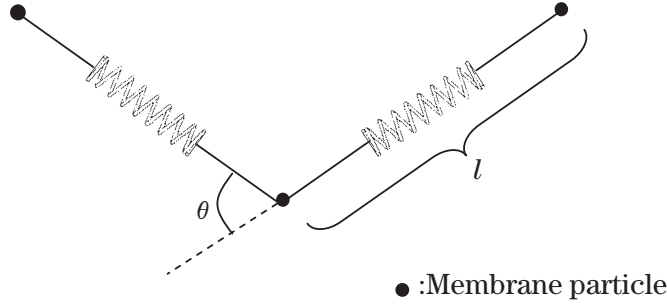


Figure 2 The elastic spring model of the RBC membrane

membrane particles connecting with the neighboring membrane particles by springs, as shown in Figure 2. Elastic energy stores in the spring due to the change of the length l of the spring with respected to its reference length l_0 and the change in angle θ between two neighboring springs. The total elastic energy of the RBC membrane, $E = E_l + E_b$, is the sum of the total elastic energy for stretch/compression and the total energy for bending which, in particular, are

$$E_l = \frac{k_l}{2} \sum_{i=1}^N \left(\frac{l_i - l_0}{l_0} \right)^2 \quad (2.8)$$

and

$$E_b = \frac{k_b}{2} \sum_{i=1}^N \tan^2 \left(\frac{\theta_i}{2} \right). \quad (2.9)$$

In equations (2.8) and (2.9), N is the total number of the spring elements, and k_l and k_b are spring constants for changes in length and bending angle, respectively.

Remark 2.3 In the process of creating the initial shape of RBCs described in [36], the RBC is assumed to be a circle of radius $R_0 = 2.8 \mu\text{m}$ initially. The circle is discretized into $N = 76$ membrane particles so that 76 springs are formed by connecting the neighboring particles. The shape change is stimulated by reducing the total area of the circle through a penalty function

$$\Gamma_s = \frac{k_s}{2} \left(\frac{s - s_e}{s_e} \right)^2, \quad (2.10)$$

where s and s_e are the time dependent area of the RBC and the equilibrium area of the RBC, respectively, and the total energy is modified as $E + \Gamma_s$. Based on the principle of virtual work, the force acting on the i th membrane particle now is

$$\mathbf{F}_i = - \frac{\partial(E + \Gamma_s)}{\partial \mathbf{r}_i}, \quad (2.11)$$

where \mathbf{r}_i is the position of the i th membrane particle. When the area is reduced, each RBC membrane particle moves on the basis of the following equation of motion:

$$m\ddot{\mathbf{r}}_i + \gamma\dot{\mathbf{r}}_i = \mathbf{F}_i \quad (2.12)$$

Here, $(\dot{})$ denotes the time derivative; m and γ represent the membrane particle mass and the membrane viscosity of the RBC. The position \mathbf{r}_i of the i th membrane particle is solved by discretizing (2.12) via a second order finite difference method. The total energy stored in the membrane decreases as the time elapses. The final shape of the RBC is obtained as the total elastic energy is minimized (see [38]). The area of the final shape has less than 0.001% difference from the given equilibrium area s_e and the length of the perimeter of the final shape has less than 0.005% difference from the circumference of the initial circle. The reduced area of an RBC in this paper is defined by $s^* = \frac{s_e}{\pi R_0^2}$.

2.3 Immersed boundary method

The immersed boundary method developed by Peskin (see, e.g., [31–33]) is employed in this study because of its distinguish features in dealing with the problem of fluid flow interacting with a flexible fluid/structure interface. Over the years, it has demonstrated its capability in study of computational fluid dynamics including blood flow. Based on the method, the boundary of the deformable structure is discretized spatially into a set of boundary nodes. The force located at the immersed boundary node $\mathbf{X} = (X_1, X_2)$ affects the nearby fluid mesh nodes $\mathbf{x} = (x_1, x_2)$ through a 2D discrete δ -function $D_h(\mathbf{X} - \mathbf{x})$:

$$\mathbf{f}_B(\mathbf{x}) = \sum \mathbf{F}_i D_h(\mathbf{X}_i - \mathbf{x}) \quad \text{for } |\mathbf{X} - \mathbf{x}| \leq 2h, \quad (2.13)$$

where h is the uniform finite element mesh size and

$$D_h(\mathbf{X} - \mathbf{x}) = \delta_h(X_1 - x_1)\delta_h(X_2 - x_2) \quad (2.14)$$

with the 1D discrete δ -functions being

$$\delta_h(z) = \begin{cases} \frac{1}{8h} \left(3 - \frac{2|z|}{h} + \sqrt{1 + \frac{4|z|}{h} - 4\left(\frac{|z|}{h}\right)^2} \right), & |z| \leq h, \\ \frac{1}{8h} \left(5 - \frac{2|z|}{h} - \sqrt{-7 + \frac{12|z|}{h} - 4\left(\frac{|z|}{h}\right)^2} \right), & h \leq |z| \leq 2h, \\ 0, & \text{otherwise.} \end{cases} \quad (2.15)$$

The movement of the immersed boundary node \mathbf{X} is also affected by the surrounding fluid and therefore is enforced by summing the velocities at the nearby fluid mesh nodes \mathbf{x} weighted by the same discrete δ -function:

$$\mathbf{U}(\mathbf{X}) = \sum h^2 \mathbf{u}(\mathbf{x}) D_h(\mathbf{X} - \mathbf{x}) \quad \text{for } |\mathbf{X} - \mathbf{x}| \leq 2h. \quad (2.16)$$

After each time step, the position of the immersed boundary node is updated by

$$\mathbf{X}_{t+\Delta t} = \mathbf{X}_t + \Delta t \mathbf{U}(\mathbf{X}_t). \quad (2.17)$$

2.4 Space approximation and time discretization

Concerning the finite element based space approximation of $\{\mathbf{u}, p\}$ in problem (2.1)–(2.6), we have used the P_1 -iso- P_2 and P_1 finite element approximation (e.g., see [20, Chapter 5]). Suppose that a rectangular computational domain $\Omega \subset R^2$ is chosen with length L , h is a space

discretization step, \mathcal{T}_h is a finite element triangulation of $\bar{\Omega}$ for velocity, and \mathcal{T}_{2h} is a twice coarser triangulation for pressure (see Figure 3). Let P_1 be the space of polynomials in two variables of degree ≤ 1 , we introduce the finite dimensional spaces:

$$W_{0h} = \left\{ \mathbf{v}_h \mid \begin{array}{l} \mathbf{v}_h \in C^0(\bar{\Omega})^2, \mathbf{v}_h|_T \in P_1 \times P_1, \forall T \in \mathcal{T}_h, \mathbf{v}_h = \mathbf{0} \text{ on the top and bottom} \\ \text{of } \Omega \text{ and is periodic in the } x_1 \text{ direction with period } L \end{array} \right\},$$

$$L_h^2 = \left\{ q_h \mid \begin{array}{l} q_h \in C^0(\bar{\Omega}), q_h|_T \in P_1, \forall T \in \mathcal{T}_{2h}, q_h \text{ is periodic in the } x_1 \\ \text{direction with period } L \end{array} \right\}.$$

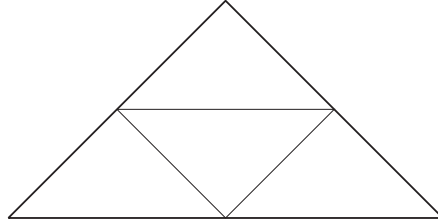


Figure 3 Schematic representation of a FEM triangulation and its subtriangulation

A finite dimensional space approximating $\Lambda_0(t)$ is defined as follows: let $\{\mathbf{x}_i\}_{i=1}^N$ be a set of points covering $\bar{B}(t)$. We define then

$$\Lambda_h(t) = \left\{ \boldsymbol{\mu}_h \mid \boldsymbol{\mu}_h = \sum_{i=1}^N \boldsymbol{\mu}_i \delta(\mathbf{x} - \mathbf{x}_i), \boldsymbol{\mu}_i \in \mathbb{R}^2, \forall i = 1, \dots, N \right\}, \quad (2.18)$$

where $\delta(\cdot)$ is the Dirac measure at $\mathbf{x} = \mathbf{0}$. Then, instead of the scalar product of $(H^1(B(t)))^2$, we shall use $\langle \cdot, \cdot \rangle_{B_h(t)}$ defined by

$$\langle \boldsymbol{\mu}_h, \mathbf{v}_h \rangle_{B_h(t)} = \sum_{i=1}^N \boldsymbol{\mu}_i \cdot \mathbf{v}_h(\mathbf{x}_i), \quad \forall \boldsymbol{\mu}_h \in \Lambda_h(t), \mathbf{v}_h \in W_{0,h}. \quad (2.19)$$

Then we approximate $\Lambda_0(t)$ by

$$\Lambda_{0,h}(t) = \{ \boldsymbol{\mu}_h \mid \boldsymbol{\mu}_h \in \Lambda_h(t), \langle \boldsymbol{\mu}_h, \mathbf{e}_i \rangle_{B_h(t)} = 0, i = 1, 2, \langle \boldsymbol{\mu}_h, \overrightarrow{Gx^\perp} \rangle_{B_h(t)} = 0 \}. \quad (2.20)$$

A typical choice of points for defining $\Lambda_h(t)$ is to take the grid points of the velocity mesh internal to the region $B(t)$ and whose distance to the boundary of $B(t)$ is greater than, e.g. $\frac{h}{2}$, and to complete with selected points from the boundary of $B(t)$.

Then we apply the Lie's scheme (see [7, 20]) to equations (2.1)–(2.6) with the backward Euler method in time for some subproblems and obtain the following fractional step subproblems (some of the subscripts h have been dropped):

$\mathbf{u}^0 = \mathbf{u}_0$ is given. For $n \geq 0$, \mathbf{u}^n being known, we compute the approximate solution via the following fractional steps:

(1) Solve

$$\begin{cases} \rho \int_{\Omega} \frac{\mathbf{u}^{n+\frac{1}{6}} - \mathbf{u}^n}{\Delta t} \cdot \mathbf{v} \, d\mathbf{x} - \int_{\Omega} p^{n+\frac{1}{6}} (\nabla \cdot \mathbf{v}) \, d\mathbf{x} = 0, & \forall \mathbf{v} \in W_{0h}, \\ \int_{\Omega} q \nabla \cdot \mathbf{u}^{n+\frac{1}{6}} \, d\mathbf{x} = 0, & \forall q \in L_h^2, \\ \mathbf{u}^{n+\frac{1}{6}} \in W_{0h}, \quad p^{n+\frac{1}{6}} \in L_h^2. \end{cases} \quad (2.21)$$

(2) Update the position of the membrane by (2.16) and (2.17) and then compute the force \mathbf{f}_B on the fluid/cell interface by (2.11) and (2.13).

(3) Solve

$$\begin{cases} \int_{\Omega} \frac{\partial \mathbf{u}(t)}{\partial t} \cdot \mathbf{v} dx + \int_{\Omega} (\mathbf{u}^{n+\frac{1}{6}} \cdot \nabla) \mathbf{u}(t) \cdot \mathbf{v} dx = 0, & \text{on } (t^n, t^{n+1}), \quad \forall \mathbf{v} \in W_{0h}, \\ \mathbf{u}(t^n) = \mathbf{u}^{n+\frac{1}{6}}, \\ \mathbf{u}(t) \in W_{0h}, & \text{on } (t^n, t^{n+1}), \end{cases} \quad (2.22)$$

and set $\mathbf{u}^{n+\frac{2}{6}} = \mathbf{u}(t^{n+1})$.

(4) Next, compute $\mathbf{u}^{n+\frac{3}{6}}$ via the solution of

$$\begin{cases} \rho \int_{\Omega} \frac{\mathbf{u}^{n+\frac{3}{6}} - \mathbf{u}^{n+\frac{2}{6}}}{\Delta t} \cdot \mathbf{v} dx + \mu \int_{\Omega} \nabla \mathbf{u}^{n+\frac{3}{6}} : \nabla \mathbf{v} dx = 0, \\ \forall \mathbf{v} \in W_{0,h}, \quad \mathbf{u}^{n+\frac{3}{6}} \in W_{0,h}. \end{cases} \quad (2.23)$$

(5) Now predict the position and the translation velocity of the center of mass of the particles as follows:

Take $\mathbf{V}_{\mathbf{G}}^{n+\frac{4}{6},0} = \mathbf{V}_{\mathbf{G}}^n$ and $\mathbf{G}^{n+\frac{4}{6},0} = \mathbf{G}^n$. Then predict the new position of the particle via the following subcycling and predicting-correcting technique:

For $k = 1, \dots, N$, compute

$$\widehat{\mathbf{V}}_{\mathbf{G}}^{n+\frac{4}{6},k} = \mathbf{V}_{\mathbf{G}}^{n+\frac{4}{6},k-1} + \mathbf{F}^r(\mathbf{G}^{n+\frac{4}{6},k-1}) \frac{\Delta t}{2N}, \quad (2.24)$$

$$\widehat{\mathbf{G}}^{n+\frac{4}{6},k} = \mathbf{G}^{n+\frac{4}{6},k-1} + (\widehat{\mathbf{V}}_{\mathbf{G}}^{n+\frac{4}{6},k} + \mathbf{V}_{\mathbf{G}}^{n+\frac{4}{6},k-1}) \frac{\Delta t}{4N}, \quad (2.25)$$

$$\mathbf{V}_{\mathbf{G}}^{n+\frac{4}{6},k} = \mathbf{V}_{\mathbf{G}}^{n+\frac{4}{6},k-1} + (\mathbf{F}^r(\widehat{\mathbf{G}}^{n+\frac{4}{6},k}) + \mathbf{F}^r(\mathbf{G}^{n+\frac{4}{6},k-1})) \frac{\Delta t}{4N}, \quad (2.26)$$

$$\mathbf{G}^{n+\frac{4}{6},k} = \mathbf{G}^{n+\frac{4}{6},k-1} + (\mathbf{V}_{\mathbf{G}}^{n+\frac{4}{6},k} + \mathbf{V}_{\mathbf{G}}^{n+\frac{4}{6},k-1}) \frac{\Delta t}{4N}, \quad (2.27)$$

enddo;

$$\text{and let } \mathbf{V}_{\mathbf{G}}^{n+\frac{4}{6}} = \mathbf{V}_{\mathbf{G}}^{n+\frac{4}{6},N}, \quad \mathbf{G}^{n+\frac{4}{6}} = \mathbf{G}^{n+\frac{4}{6},N}. \quad (2.28)$$

(6) Now, compute $\mathbf{u}^{n+\frac{5}{6}}$, $\boldsymbol{\lambda}^{n+\frac{5}{6}}$, $\mathbf{V}_{\mathbf{G}}^{n+\frac{5}{6}}$ and $\omega^{n+\frac{5}{6}}$ via the solution of

$$\begin{cases} \rho \int_{\Omega} \frac{\mathbf{u}^{n+\frac{5}{6}} - \mathbf{u}^{n+\frac{4}{6}}}{\Delta t} \cdot \mathbf{v} dx = \langle \boldsymbol{\lambda}, \mathbf{v} \rangle_{B_h^{n+\frac{4}{6}}}, & \forall \mathbf{v} \in W_{0,h}, \\ \langle \boldsymbol{\mu}, \mathbf{u}^{n+\frac{5}{6}} \rangle_{B_h^{n+\frac{4}{6}}} = 0, & \forall \boldsymbol{\mu} \in \Lambda_{0,h}^{n+\frac{4}{6}}, \quad \mathbf{u}^{n+\frac{5}{6}} \in W_{0,h}, \quad \boldsymbol{\lambda}^{n+\frac{5}{6}} \in \Lambda_{0,h}^{n+\frac{4}{6}}, \end{cases} \quad (2.29)$$

and solve for $\mathbf{V}_{\mathbf{G}}^{n+\frac{5}{6}}$ and $\omega^{n+\frac{5}{6}}$ from

$$\begin{cases} \langle \mathbf{e}_i, \mathbf{u}^{n+\frac{5}{6}} - \mathbf{V}_{\mathbf{G}}^{n+\frac{5}{6}} - \omega^{n+\frac{5}{6}} \overrightarrow{G^{n+\frac{4}{6}}x} \rangle_{B_h^{n+\frac{4}{6}}} = 0 & \text{for } i = 1, 2, \\ \langle \overrightarrow{G^{n+\frac{4}{6}}x}, \mathbf{u}^{n+\frac{5}{6}} - \mathbf{V}_{\mathbf{G}}^{n+\frac{5}{6}} - \omega^{n+\frac{5}{6}} \overrightarrow{G^{n+\frac{4}{6}}x} \rangle_{B_h^{n+\frac{4}{6}}} = 0. \end{cases} \quad (2.30)$$

(7) Finally, take $\mathbf{V}_{\mathbf{G}}^{n+1,0} = \mathbf{V}_{\mathbf{G}}^{n+\frac{5}{6}}$ and $\mathbf{G}^{n+1,0} = \mathbf{G}^{n+\frac{4}{6}}$. Then predict the final position and translation velocity as follows:

For $k = 1, \dots, N$, compute

$$\widehat{\mathbf{V}}_{\mathbf{G}}^{n+1,k} = \mathbf{V}_{\mathbf{G}}^{n+1,k-1} + \mathbf{F}^r(\mathbf{G}^{n+1,k-1}) \frac{\Delta t}{2N}, \tag{2.31}$$

$$\widehat{\mathbf{G}}^{n+1,k} = \mathbf{G}^{n+1,k-1} + (\widehat{\mathbf{V}}_{\mathbf{G}}^{n+1,k} + \mathbf{V}_{\mathbf{G}}^{n+1,k-1}) \frac{\Delta t}{4N}, \tag{2.32}$$

$$\mathbf{V}_{\mathbf{G}}^{n+1,k} = \mathbf{V}_{\mathbf{G}}^{n+1,k-1} + (\mathbf{F}^r(\widehat{\mathbf{G}}^{n+1,k}) + \mathbf{F}^r(\mathbf{G}^{n+1,k-1})) \frac{\Delta t}{4N}, \tag{2.33}$$

$$\mathbf{G}^{n+1,k} = \mathbf{G}^{n+1,k-1} + (\mathbf{V}_{\mathbf{G}}^{n+1,k} + \mathbf{V}_{\mathbf{G}}^{n+1,k-1}) \frac{\Delta t}{4N}, \tag{2.34}$$

enddo;

and let $\mathbf{V}_{\mathbf{G}}^{n+1} = \mathbf{V}_{\mathbf{G}}^{n+1,N}$, $\mathbf{G}^{n+1} = \mathbf{G}^{n+1,N}$;

and set $\mathbf{u}^{n+1} = \mathbf{u}^{n+\frac{5}{6}}$, $\omega^{n+1} = \omega^{n+\frac{5}{6}}$.

In the above algorithm (2.21)–(2.34), we have that $t^{n+s} = (n+s)\Delta t$, $\Lambda_{0,h}^{n+s} = \Lambda_{0,h}(t^{n+s})$, B_h^{n+s} is the region occupied by the particle centered at \mathbf{G}^{n+s} , and \mathbf{F}^r is a short range repulsion force which prevents the particle/particle and particle/wall penetration (see, e.g., [21]).

The degenerated quasi-Stokes problem (2.21) is solved by a preconditioned conjugate gradient method (see, e.g., [20]), in which discrete elliptic problems from the preconditioning are solved by a matrix-free fast solver from FISHPAK by Adams et al. in [1]. The advection problem (2.22) for the velocity field is solved by a wave-like equation method as in [10] and [11]. Problem (2.23) is a classical discrete elliptic problem which can be solved by the same matrix-free fast solver. To enforce the rigid body motion inside the region occupied by the neutrally buoyant particles, we have applied the conjugate gradient method discussed in [29] to solve problem (2.29).

Remark 2.4 When simulating the case involving both cells and neutrally buoyant particles, we do need a repulsive force to prevent the overlapping between cell and particle. The repulsive force is obtained from the following Morse potential (see, e.g., [2]) $\phi(s) = k_r(1 - e^{-(s-s_0)})^2$ where the parameter s is the shortest distance between the membrane particle and the surface of the solid particle and s_0 is the range of the repulsive force (when the distance s is greater than s_0 , there is no repulsive force). The parameter k_r is a constance for the strength of the potential. At step (2) in the above algorithm (2.21)–(2.34), we then also compute $\mathbf{f}_r = -\frac{\partial\phi(s)}{\partial s}$ for each membrane particle which is close to a solid particle.

Remark 2.5 In algorithm (2.21)–(2.34), we can only use steps 1 to 4 for simulating the motion of cells in Poiseuille flow when there are no neutrally buoyant particles. Also when simulating the motion of neutrally buoyant disks in Poiseuille flow without any cells, we just skip step (2) in algorithm (2.21)–(2.34) and then obtain the one in [29].

3 Numerical Results and Discussions

In [38], we have validated the immersed boundary method with the elastic spring model by

comparing the numerical results with previous experimental data (see [19]), theoretical Keller and Skalak model (see [24]), and simulations (see [5, 26]) for the inclination angles and tank-treading frequencies of single RBC in shear flow. In this paper, the lateral migration properties of many cells in Poiseuille flows have been investigated. We have validated it by comparing the size of the cell-free layer next to the walls with the ones obtained in [6, 9]. Then we have combined the methodology with a distributed Lagrange multiplier/fictitious domain method to simulate the interaction of cells and neutrally buoyant particles in a microchannel (see, e.g., [17, 25], for cardiovascular and oncological applications). The computational results show that the neutrally buoyant disks behave similar to the almost circular cells when interacting with other cells.

The initial shapes of cells used in the flow simulations in this paper are obtained via the procedure described in [38] and Remark 2.3. We have chosen the same values of parameters for modelling cells used in [36] as follows: The bending constant in (2.9) is $k_b = 5 \times 10^{-10}$ N · m, the spring constant in (2.8) is $k_l = 5 \times 10^{-8}$ N · m, and the penalty coefficient in (2.10) is $k_s = 10^{-5}$ N · m. The cells are suspended in blood plasma which has a density $\rho = 1.00$ g/cm³ and a dynamical viscosity $\mu = 0.012$ g/(cm · s). The viscosity ratio which describes the viscosity contrast of the fluid inside and outside the RBC membrane is fixed at 1.0. The computational domain is a two dimensional horizontal channel. In the simulation, a constant pressure gradient is prescribed as a body force. In addition, periodic conditions are imposed at the left and right boundary of the domain. The Reynolds number is defined by $Re = \rho UH/\mu$ where U is the averaged velocity in the channel and H is the height of the channel.

3.1 Migration of many cells in Poiseuille flow

To apply the methodology to many cell cases, we have first considered the cases of 50 and 100 RBCs of reduced area $s^* = 0.7$ in a Poiseuille flow. The fluid domain is $100 \mu\text{m} \times 50 \mu\text{m}$. Hence, the hematocrit of the 50 cell case (resp., 100 cell case) is $\text{Hct} = 17.24\%$ (resp., $\text{Hct} = 34.48\%$). The pressure gradient is set as constant for this study so that the averaged velocity U of the Poiseuille flow without cells is 6.666 cm/sec. The initial velocity is zero everywhere. The grid resolution for the computational domain is 32 grid points per $10 \mu\text{m}$. The time step is 0.00001 ms. The positions and shapes of cells at different times are shown in Figures 4 and 5. We have observed that the cells move toward the center of the channel, an effect attributed to their deformability. Similar two-dimensional results have been observed numerically in [3, 9]. There are cell-free layers next to the walls as shown in Figures 4 and 5. In [6], the cell-free layer has been estimated to be roughly $100/\text{Hct}$ in cylindrical tubes with diameters between 40 and 83 μm . In [9], the numerical results of the size of the cell-free layer are in agreement with the above estimation reported in [6]. Thus for $\text{Hct} = 17.24\%$, the estimation of the cell-free layer is about 5.8 μm (and 2.9 μm for the $\text{Hct} = 34.48\%$ case). Our results show the averaged size of cell-free layer is about 6.24 μm (resp., 2.94 μm) for the $\text{Hct} = 17.24\%$ case (resp., the $\text{Hct} = 34.48\%$ case), which are in agreement with the estimation in [6]. The Reynolds number based the averaged velocity and the channel height for the 50 cell case (resp., 100 cell case) is about $Re = 2.346$ (resp., $Re = 1.677$).

Then we consider the cases where the averaged velocity is reduced to $U = 3.333$ cm/sec and

all other parameters are kept the same. The positions and shapes of cells are shown in Figure 6. The computational results show the averaged size of cell-free layer is about $5.92 \mu\text{m}$ (resp., $2.97 \mu\text{m}$) for the $\text{Hct} = 17.24\%$ case (resp., the $\text{Hct} = 34.48\%$ case), which are in agreement with the estimation in [6]. The Reynolds number based the averaged velocity and the channel height for the 50 cell case (resp., 100 cell case) is about $Re = 1.17$ (resp., $Re = 0.867$).

In Figures 4 to 6, the orientation of cells has shown some symmetry with respect to the center line of the channel. Since the two channel walls are at rest, the cell located between the center line and a wall is in a kind of “nonlinear shear” flow. Hence, the motion and inclination angles of those cells are similar to the behavior of cell migrating in a “linear shear” flow between two parallel plates, which is that the cell migrates to the center line with an inclination angle related to the reduced area of the cell.

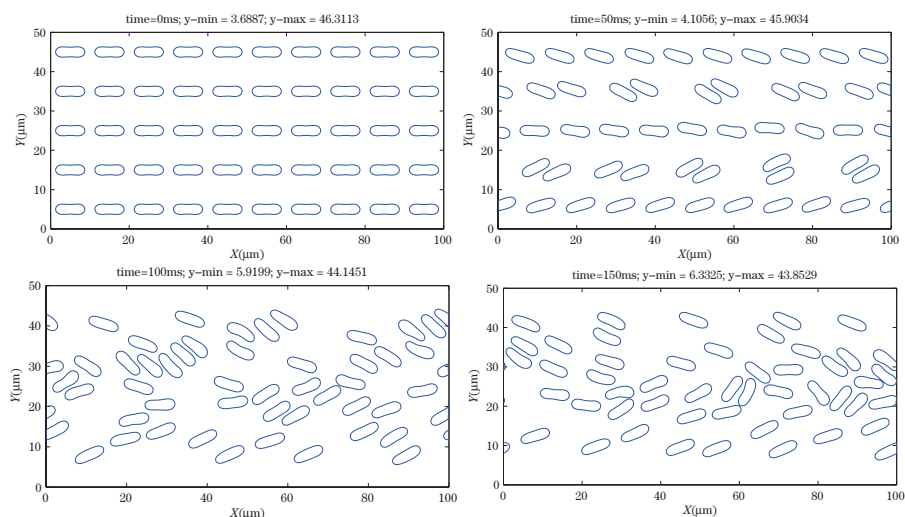


Figure 4 The shape and the position of 50 cells for $U = 6.666 \text{ cm/sec}$ at $t = 0, 50, 100$ and 150 ms

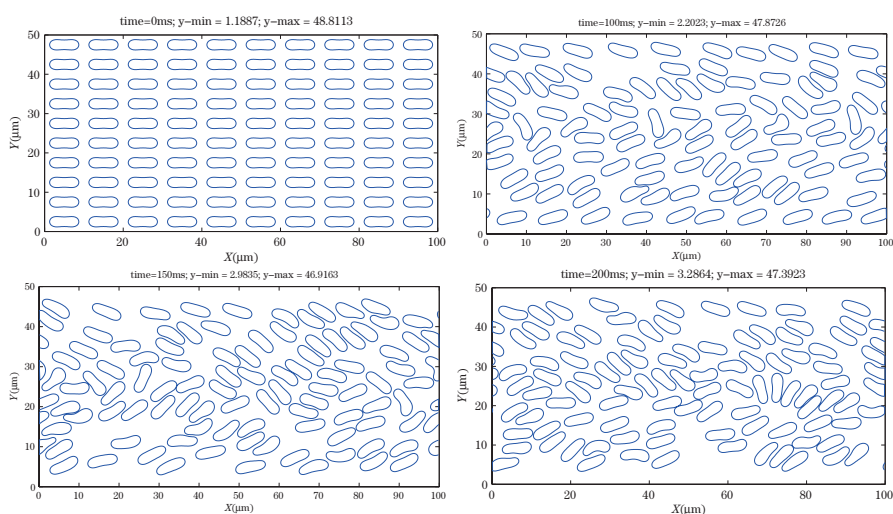


Figure 5 The shape and the position of 100 cells for $U = 6.666 \text{ cm/sec}$ at $t = 0, 100, 150$ and 200 ms

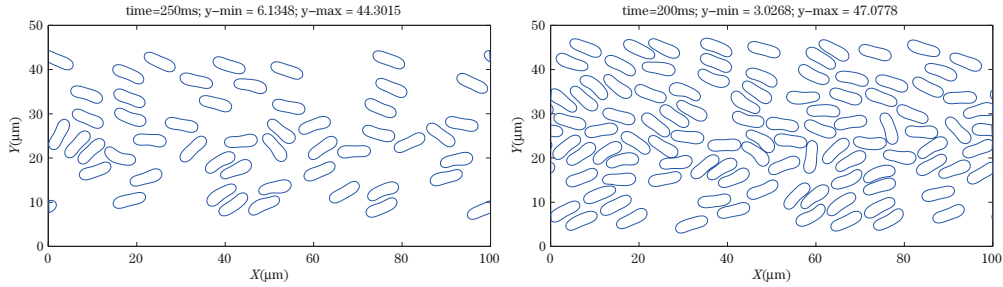


Figure 6 The shape and the position of 50 cells at $t = 250$ ms (left) and those of 100 cells (right) at $t = 200$ ms for $U = 3.333$ cm/sec

3.2 Interaction of two kinds of cells in Poiseuille flow

In this section, we have simulated the interaction of cells of two reduced areas, $s^* = 0.7$ and 1, in Poiseuille flow. The cell of $s^* = 1$ is treated as a solid particle in the simulation by adjusting its bending parameter to 1000 times of the k_b , given at the beginning of Section 3. We consider the cases of forty eight cells of reduced areas $s^* = 0.7$ and two cells of reduced areas $s^* = 1$ with the averaged velocity $U = 3.333$ cm/sec. All other parameters are kept the same. The hematocrit of fifty cells is $Hct = 17.536\%$, so the estimation of the cell-free layer is about $5.7 \mu\text{m}$. We consider two cases which have different initial position of the circular cells. The positions and shapes of cells at different times are shown in Figures 7 and 8. The histories of the height of two cells of $s^* = 1$ are shown in Figure 9. Two cells of $s^* = 1$, which have almost circular shape, move to the region next to the walls and stay there, which is what we expect for such type of cells since the cell of $s^* = 1$ has less deformability and the lowest rate of migration toward the center line of the channel. Once they are in the region next to the walls, the other cells keep them in the same region. Our results show the averaged sizes of cell-free layer associated to the cells of $s^* = 0.7$ are about $5.84 \mu\text{m}$ and $6.13 \mu\text{m}$, respectively. The Reynolds numbers based the averaged velocity and the channel height are about $Re = 1.11$ and 1.08 , respectively.

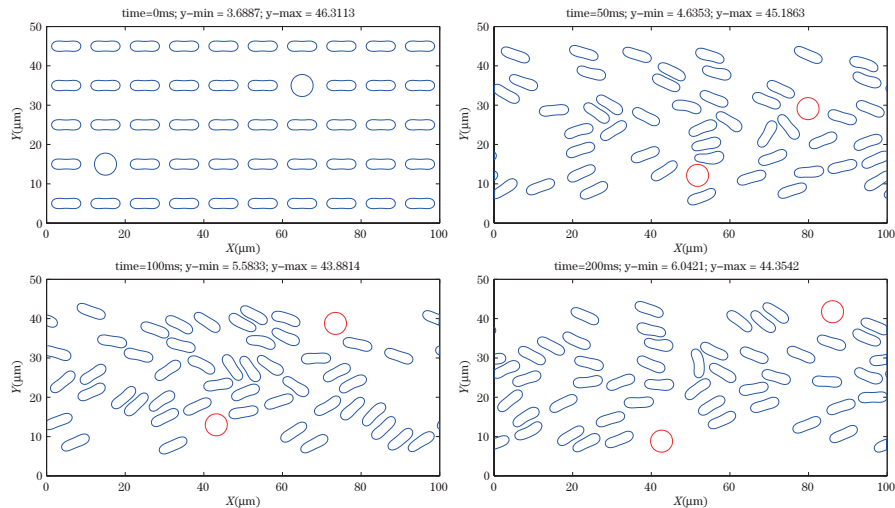


Figure 7 The shape and the position of cells for the case I at $t=0, 50, 100$ and 200 ms (from left to right and from top to bottom)

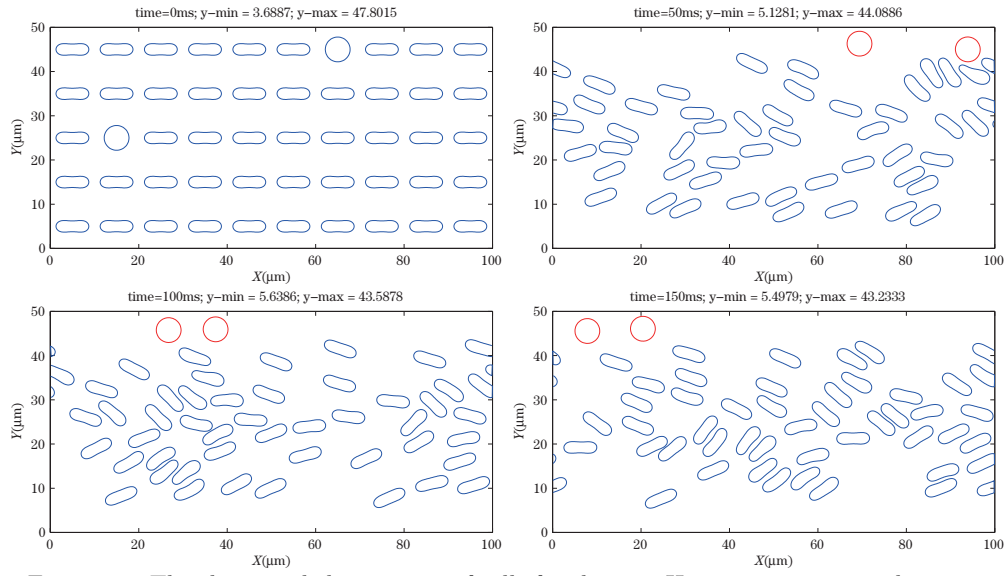


Figure 8 The shape and the position of cells for the case II at $t=0, 50, 100$ and 150 ms (from left to right and from top to bottom)

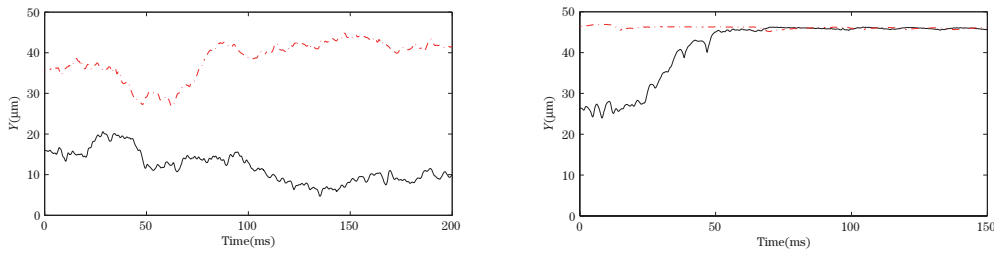


Figure 9 The histories of the height of two cells of $s^* = 1$: the case I (left) and the case II (right)

3.3 Interaction of cells and neutrally buoyant disks in Poiseuille flow

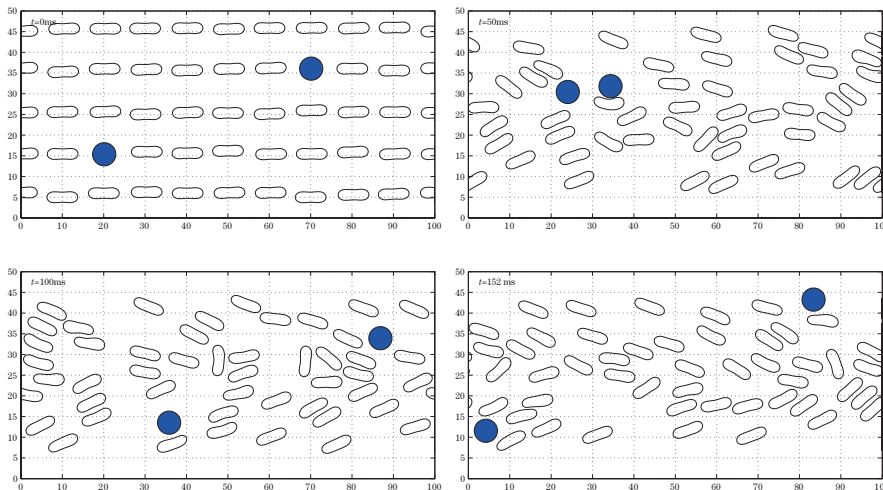


Figure 10 The shape and the position of cells and the position of two neutrally buoyant disks at $t=0, 50, 100$ and 152 ms (from left to right and from top to bottom)

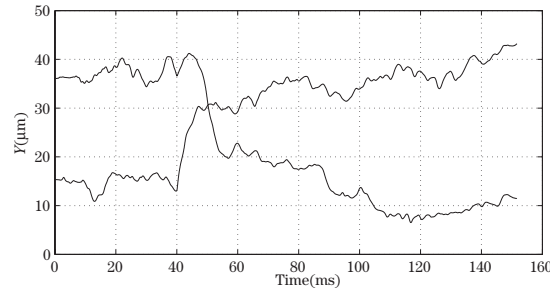


Figure 11 The histories of the height of two neutrally buoyant disks

In this section, we simulate the interaction of forty eight cells of reduced area $s^* = 0.7$ and two neutrally buoyant disks of radius $2.8 \mu\text{m}$ in Poiseuille flow. We keep all other parameters the same as those in Section 3.2. The parameter k_r for the repulsive force is $k_r = 1 \times 10^{-9} \text{ N} \cdot \text{m}$. The range of the repulsive force is two times of the meshsize for the velocity field. The positions and shapes of cells and disks at different times are shown in Figure 10. The histories of the height of two neutrally buoyant disks are shown in Figure 11. The two neutrally buoyant disks behaves similar to those two almost circular cells discussed in Section 3.2. The interaction with cells keeps them in the region next to the walls. We will report further study of the interaction of cells and particles in the near future.

4 Conclusions

In summary, a numerical model is tested in this paper for simulating the motion of many RBCs in Poiseuille flows. For many cell cases, our results show that the size of the cell-free layer is in agreement with the estimation in [6] for the different values of Hct and the averaged velocities. Also the circular cells like to move the region next to the wall which is similar to the behavior of white blood cells in microvessels. For the interaction of cells and neutrally buoyant disks, the computational results show that the neutrally buoyant disks behave similar to the almost circular cells when interacting with other cells. The numerical results in this paper are quantitatively/qualitatively similar to experimental observations and other investigators' findings thus show the potential of this numerical algorithm for future studies of blood flow in microcirculation and microchannels.

Acknowledgement The authors acknowledge the helpful comments of James Feng, Ming-Chih Lai and Sheldon X. Wang.

References

- [1] Adams, J., Swarztrauber, P. and Sweet, R., FISHPAK: A package of Fortran subprograms for the solution of separable elliptic partial differential equations, The National Center for Atmospheric Research, Boulder, Colorado, 1980.
- [2] Alexeev, A., Verberg, R. and Balazs, A. C., Modeling the interactions between deformable capsules rolling on a compliant surface, *Soft Matter*, **2**, 2006, 499–509.
- [3] Bagchi, P., Mesoscale simulation of blood flow in small vessels, *Biophys. J.*, **92**, 2007, 1858–1877.
- [4] Bagchi, P., Johnson, P. and Popel, A., Computational fluid dynamic simulation of aggregation of deformable cells in a shear flow, *J. Biomech. Eng.*, **127**, 2005, 1070–1080.

- [5] Beaucourt, J., Rioual, F., Séon, T., et al., Steady to unsteady dynamics of a vesicle in a flow, *Phys. Rev. E*, **9**, 2004, 011906.
- [6] Blackshear, P. Jr, Forstorm, R., Dorman, F. and Voss, G., Effect of flow on cells near walls, *Federal Proceedings*, **30**, 1971, 1600–1609.
- [7] Chorin, A. J., Hughes, T. J. R., McCracken, M. F. and Marsden, J. E., Product formulas and numerical algorithms, *Comm. Pure Appl. Math.*, **31**, 1978, 205–256.
- [8] Cristini, V. and Kassab, G. S., Computer modeling of red blood cell rheology in the microcirculation: a brief overview, *Ann. Biomed. Eng.*, **33**, 2005, 1724–1727.
- [9] Crowl, L. M. and Fogelson, A. L., Computational model of whole blood exhibiting lateral platelet motion induced by red blood cells, *Int. J. Numer. Meth. Biomed. Engng.*, **26**, 2009, 471–487.
- [10] Dean, E. J. and Glowinski, R., A wave equation approach to the numerical solution of the Navier-Stokes equations for incompressible viscous flow, *C.R. Acad. Sc. Paris, Série 1*, **325**, 1997, 783–791.
- [11] Dean, E. J., Glowinski, R. and Pan, T. W., A wave equation approach to the numerical simulation of incompressible viscous fluid flow modeled by the NavierStokes equations, *Mathematical and Numerical Aspects of Wave Propagation*, De Santo, J. A. (ed.), SIAM, Philadelphia, 1998, 65–74.
- [12] Dubus, C. and Fournier, J. B., A Gaussian model for the membrane of red blood cells with cytoskeletal defects, *Europhys. Lett.*, **75**, 2006, 181–187.
- [13] Dupin, M. M., Halliday, I., Care, C. M., et al., Modeling the flow of dense suspensions of deformable particles in three dimensions, *Phys. Rev. E*, **75**, 2007, 066707.
- [14] Dzwiniel, W., Boryczko, K. and Yuen, D., A discrete-particle model of blood dynamics in capillary vessels, *J. Colloid Interface Sci.*, **258**, 2003, 163173.
- [15] Eggleton, C. and Popel, A., Large deformation of red blood cell ghosts in a simple shear flow, *Phys. Fluids*, **10**, 1998, 1834–1845.
- [16] Fahraeus, R. and Lindqvist, T., The viscosity of blood in narrow capillary tubes, *Am. J. of Physiol.*, **96**, 1931, 562–568.
- [17] Ferrari, M., Cancer nanotechnology: opportunities and challenges, *Nat. Rev. Cancer*, **5**, 2005, 161–171.
- [18] Fischer, T. M., Shape memory of human red blood cells, *Biophys. J.*, **86**, 2004, 3304–3313.
- [19] Fischer, T. M., Stöhr-Liesen, M. and Schmid-Schönbein, H., The red cell as a fluid droplet: tank tread-like motion of the human erythrocyte membrane in shear flow, *Science*, **202**, 1978, 894–896.
- [20] Glowinski, R., Finite element methods for incompressible viscous flow, *Handbook of Numerical Analysis*, Vol. IX, Ciarlet, P. G. and Lions, J. L. (eds.), North-Holland, Amsterdam, 2003, 7–1176.
- [21] Glowinski, R., Pan, T. W., Hesla, T., et al., A fictitious domain approach to the direct numerical simulation of incompressible viscous flow past moving rigid bodies: application to particulate flow, *J. Comput. Phys.*, **169**, 2001, 363–427.
- [22] Hansen, J. C., Skalak, S. and Hoger, A., An elastic network model based on the structure of the red blood cell membrane skeleton, *Biophys. J.*, **70**, 1996, 146–166.
- [23] Hosseini, S. M. and Feng, J. J., A particle-based model for the transport of erythrocytes in capillaries, *Chem. Engng. Sci.*, **64**, 2009, 4488–4497.
- [24] Keller, S. R. and Skalak, R., Motion of a tank-treading ellipsoidal particle in a shear flow, *J. Fluid Mech.*, **120**, 1982, 27–47.
- [25] La Van, A. D., Mcguire, T. M. and Langer, R., Small-scale systems for in vivo drug delivery, *Nat. Biotech.*, **21**, 2003, 1184–1191.
- [26] Li, H. B., Yi, H. H., Shan, X. W. and Fang, H. P., Shape changes and motion of a vesicle in a fluid using a lattice Boltzmann model, *Europhysics Letters*, **81**, 2008, 54002.
- [27] Liu, L. and Liu, W. K., Rheology of red blood cell aggregation by computer simulation, *J. Comput. Phys.*, **220**, 2006, 139–154.
- [28] Liu, W. K., Liu, Y., Farrell, D., et al., Immersed finite element method and its applications to biological systems, *Comput. Methods Appl. Mech. Eng.*, **195**, 2006, 1722–1749.
- [29] Pan, T. W. and Glowinski, R., Direct simulation of the motion of neutrally buoyant circular cylinders in plane Poiseuille flow, *J. Comput. Phys.*, **181**, 2002, 260–279.
- [30] Pan, T. W., Joseph, D. D., Bai, R., et al., Fluidization of 1204 spheres: simulation and experiments, *J. Fluid Mech.*, **451**, 2002, 169–191.
- [31] Peskin, C. S., Numerical analysis of blood flow in the heart, *J. Comput. Phys.*, **25**, 1977, 220–252.

- [32] Peskin, C. S., The immersed boundary method, *Acta Numer.*, **11**, 2002, 479–517.
- [33] Peskin, C. S. and McQueen, D. M., Modeling prosthetic heart valves for numerical analysis of blood flow in the heart, *J. Comput. Phys.*, **37**, 1980, 11332.
- [34] Pozrikidis, C., *Modeling and Simulation of Capsules and Biological Cells*, Chapman & Hall/CRC, Boca Raton, 2003.
- [35] Secomb, T. W., Styp-Rekowska, B. and Pries, A. R., Two-dimensional simulation of red blood cell deformation and lateral migration in microvessels, *Ann. Biomed. Eng.*, **35**, 2007, 755–765.
- [36] Tsubota, K., Wada, S. and Yamaguchi, T., Simulation study on effects of hematocrit on blood flow properties using particle method, *J. Biomech. Sci. Eng.*, **1**, 2006, 159–170.
- [37] Vera, C., Skelton, R., Bossens, F. and Sung, L. A., 3-D nanomechanics of an erythrocyte junctional complex in equibiaxial and anisotropic deformations, *Ann. Biomed. Eng.*, **33**, 2005, 1387–1404.
- [38] Wang, T., Pan, T. W., Xing, Z. and Glowinski, R., Numerical simulation of rheology of red blood cell rouleaux in microchannels, *Phys. Rev. E*, **79**, 2009, 041916.